ACS APPLIED MATERIALS & INTERFACES

Research Article

Modification of Graphene Oxide/V$_2$O$_5$·nH$_2$O Nanocomposite Films via Direct Laser Irradiation

Algirdas Lazauskas,* Liutauras Marcinauskas, and Mindaugas Andrulevicius

Cite This: *ACS Appl. Mater. Interfaces* 2020, 12, 18877−18884

Read Online

ACCESS | Metrics & More | Article Recommendations | SI Supporting Information

ABSTRACT: Herein, photothermal modification of nanocomposite films consisting of hydrated vanadium pentoxide (V$_2$O$_5$·nH$_2$O) nanoribbons wrapped with graphene oxide (GO) flakes was performed via 405 nm direct laser irradiation. The combination of X-ray diffraction, X-ray photoelectron spectroscopy, Raman scattering, transmission electron microscopy, and scanning electron microscopy allowed comprehensive characterization of physical and chemical changes of GO/V$_2$O$_5$·nH$_2$O nanocomposite films upon photothermal modification. The modified nanocomposite films exhibited porous surface morphology (17.27 m^2 g^{-1}) consisting of randomly distributed pillarlike protrusions. The photothermal modification process of GO/V$_2$O$_5$·nH$_2$O enhanced the electrical conductivity of nanocomposite from 1.6 to 6.8 S/m. It was also determined that the direct laser irradiation of GO/V$_2$O$_5$·nH$_2$O resulted in considerable decrease of C−O bounds as well as O−H functional groups with an increase of the laser power density.

KEYWORDS: *graphene oxide, vanadium pentoxide, photothermal modification, laser, nanocomposite, functional*
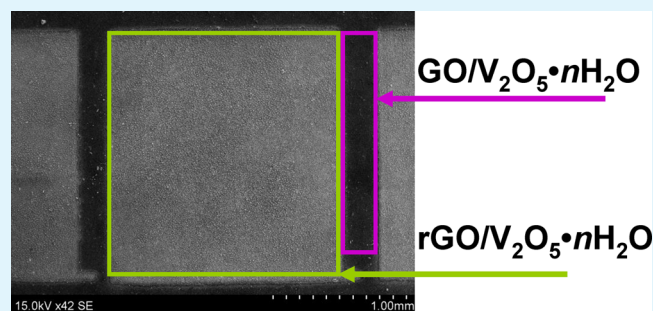
INTRODUCTION

Vanadium pentoxide (V$_2$O$_5$) has gained substantial scientific interest due to its outstanding properties in many different applications, such as lithium−ion batteries (LIB),[1,2] supercapacitors,[3,4] field-effect transistors,[5] sensors,[6−8] electrochromic devices,[9−11] and actuators.[12] This transition-metal oxide is highly valued because of its affordable cost and high energy density.[13,14] It is almost unique electrode material that is capable of hosting monovalent as well as multivalent cations. In contrast to bulk V$_2$O$_5$ properties, enhanced device performances were reported via application of V$_2$O$_5$ nanostructures, such as nanowires,[15] nanotubes,[16] nanobelts,[17] and nanorods.[18] These crystalline V$_2$O$_5$ nanostructures can be synthesized via hydrothermal, solvothermal, or sol−gel methods. Another type of this transition-metal oxide is known as hydrated vanadium pentoxide (also known as "amorphous V$_2$O$_5$" or V$_2$O$_5$ xerogel) with general formula V$_2$O$_5$·nH$_2$O (where n commonly falls in the range of 0−3). It can be characterized as a material having short-range order with an ordered stacking of VO$_5$ bilayers at nanoscale. In contract to crystalline V$_2$O$_5$ nanoderivatives, V$_2$O$_5$·nH$_2$O (as an electrode material) has been reported to exhibit higher electrochemical performance (e.g., discharge potential, energy density, and cyclic stability) owing to the fast heterogeneous charge-transfer reactions.[19,20] It is also considered that amorphous or low-crystallinity electrode materials are less prone to mechanical stress during the large cation hosting and release processes and thus can provide higher intercalation capacities than high-crystallinity ones.[19] The V$_2$O$_5$·nH$_2$O is also diversely used in other applications, such as chemical sensors,[21] electrochromic devices,[22] catalysis,[23] etc. Physical and chemical vapor deposition apart, V$_2$O$_5$·nH$_2$O is commonly synthesized via solution-based routes, such as ionic exchange from NaVO$_3$,[24] hydrolysis and condensation from alkoxide,[25] crystalline V$_2$O$_5$ reaction with peroxides,[26] or melt-quenching[27] in H$_2$O. Like most metal oxides, both V$_2$O$_5$ and V$_2$O$_5$·nH$_2$O suffer from low electrical conductivity, which limits implementation of these materials in LIB and supercapacitor applications.[28−30] A common practice is to combine nanostructured metal oxides with carbonaceous nanoderivatives, such as carbon nanotubes,[31] carbon nanofiber,[32] mesoporous carbon,[33] and graphene[34] for the enhancement of the electronic conductivity and their structural stability.[35−37] Specifically, the combination of reduced graphene oxide (rGO) with nanostructured V$_2$O$_5$ was reported to be an attractive protocol to achieve electrode materials with high electrochemical performance for supercapacitors due to
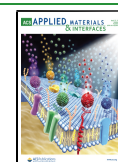
enhanced power and energy densities.[38,39] However, common methods employed to produce rGO-containing nanocomposite materials, such as hydrothermal[40] and solvothermal[34] synthesis routes are not applicable to large-scale process and lack selectivity. Therefore, exploration and development of novel strategies is meaningful in this context. Photothermal modification via direct laser irradiation is one of the most attractive protocols due to its flexible, economical, selective, and reliable patterning characteristics.[41] Importantly, it was shown that this protocol allows to obtain the graphene-like materials with high sp^2 content.[42] Furthermore, the direct laser irradiation process is highly tunable and allows one to achieve different physical and chemical characteristics of the material.[43] Based on the above, photothermal modification via direct laser irradiation is a promising strategy to prepare rGO/V$_2$O$_5$ or rGO/V$_2$O$_5$·nH$_2$O nanocomposite materials.[44]

Hereby, we reported on the photothermal modification of nanocomposite films consisting of hydrated vanadium pentoxide (V$_2$O$_5$·nH$_2$O) wrapped with graphene oxide (GO) flakes through 405 nm direct laser irradiation. The laser modified areas in the GO/V$_2$O$_5$·nH$_2$O films are defined as rGO/V$_2$O$_5$·nH$_2$O. We have demonstrated that the method applied produces porous surface morphology of rGO/V$_2$O$_5$· nH$_2$O. As it will be shown below, the morphological evolution of surface features is dependent on laser power density (LPD). The combination of X-ray diffraction (XRD), X-ray photo-electron spectroscopy (XPS), Raman scattering, transmission electron microscopy (TEM), and scanning electron micros-copy (SEM) analytical techniques allowed comprehensive characterization of physical and chemical changes of GO/ V$_2$O$_5$·nH$_2$O nanocomposite films upon photothermal mod-ification. General tendencies of changes in the functional groups depending on LPD were revealed.

■ RESULTS AND DISCUSSION

Characterization of Crystalline V$_2$O$_5$ and V$_2$O$_5$·nH$_2$O. The diffraction patterns of the crystalline V$_2$O$_5$ and V$_2$O$_5$· nH$_2$O powders are shown in Figure S1. For the fitting procedure, the crystallographic information files (CIF) of crystalline V$_2$O$_5$ and V$_2$O$_5$·nH$_2$O were assembled from refs 45 and 27, respectively. The V$_2$O$_5$ (Figure S1a) has a typical orthorhombic lattice (Crystallography Open Database (COD) ID 9012220), space group *Pmn* 21 (group number = 31) with a cell parameters a = 11.503 Å, b = 4.368 Å, c = 3.561 Å, $\alpha = \beta = \gamma = 90°$ and the (−2 0 0), (0 −1 0), (−1 −1 0), (−2 −1 0), (−1 0 −1), (−3 −1 0), (0 −1 −1), (−1 −1 −1), (−3 0 −1), (−2 −1 −1), (−4 −1 0), (0 −2 0), (−1 −2 0), (−2 −2 0), (−4 −1 −1), (−6 0 0), (−3 −2 0), (−1 −2 −1) reflexes observable in the range of 3.0−50.0°. The melt-quenching process of crystalline V$_2$O$_5$ resulted in formation of V$_2$O$_5$· nH$_2$O (Figure S1b) with a monoclinic lattice (COD ID 4124512), space group *C*12/*m*1 (group number = 12) with a cell parameters a = 11.700 Å, b = 3.617 Å, c = 11.447 Å, $\alpha = \gamma = 90°$, $\beta = 88.07°$ and the (0 0 1), (1 1 0) reflexes observable. The broad and pronounced (0 0 1) reflex of V$_2$O$_5$·nH$_2$O indicates lamellar ordering (albeit turbostatic) and is consistent with those reported elsewhere.[27] The crystallite size for the corresponding reflex was determined to be 51.2 Å. The interplanar spacing (d-spacing) of the (0 0 1) reflex was determined to be 11.7 Å. It is known that the d-spacing in V$_2$O$_5$·nH$_2$O varies depending on the amount of H$_2$O intercalated between V$_2$O$_5$ layers.[46,47] The amount of H$_2$O molecules, n, evaluated from d-spacing of the (0 0 1) reflex was

determined to be n = 1.7, which was found to be higher than V$_2$O$_5$·nH$_2$O prepared using ion exchange[48] with thermal treatment at 150 °C (n = 1.1) or alkoxide sol−gel[49] routes (n = 0.9, for sample subjected to atmospheric hydrolysis; n = 1.5, for sample prepared with pH = 1) reported previously. Several works reported that the amount of H$_2$O can considerably change the structural properties of V$_2$O$_5$· nH$_2$O.[8,17,50,51] It is known that up to 250 °C H$_2$O loss is reversible, while between 250 °C and 320−350 °C, H$_2$O molecules are removed from the lattice without a chance to be absorbed afterward at room temperature conditions, resulting in V$_2$O$_5$·0.1H$_2$O; at 350 °C and above, V$_2$O$_5$ crystallizes into Shcherbinaite with the orthorhombic structure.[52,53]

The structure information on crystalline V$_2$O$_5$ and V$_2$O$_5$· nH$_2$O was further obtained via Raman scattering, as depicted in Figure S2. The Raman spectrum of crystalline V$_2$O$_5$ (Figure S2a) exhibits a number of bands among which the band located at 994 cm^{-1} is attributed to the V=O stretching vibration.[54] The V−O stretching vibration is located at 702 cm^{-1}.[55] The band at 528 cm^{-1} is attributed to the V$_3$−O stretching vibration.[56] The V−O−V bending vibrations are observed at 482, 405, and 304 cm^{-1}.[55,57] The band at 284 cm^{-1} is assigned to V=O bending vibration.[56−58] The O−V− O bending vibration is observed at 197 cm^{-1}.[59] The V−O−V skeleton bending vibration is observed at 145 cm^{-1}.[55,59] Similar vibrational modes of functional groups can be observed in the Raman spectrum of V$_2$O$_5$·nH$_2$O (Figure S2b). In contrast to V$_2$O$_5$, the observed bands in V$_2$O$_5$·nH$_2$O spectrum exhibit broadening and their positions are slightly shifted due to water intercalation.

The XPS was employed for the analysis of the chemical properties of crystalline V$_2$O$_5$ and V$_2$O$_5$·nH$_2$O. Figure S3 shows the XPS V 2p and O 1s high-resolution spectra with deconvoluted components. Because of the orbital splitting, the energy level of V 2p splits into the V 2p$_{3/2}$ and V 2p$_{1/2}$. The deconvoluted components in the XPS V 2p$_{3/2}$ and V 2p$_{1/2}$ high-resolution spectra of crystalline V$_2$O$_5$ and V$_2$O$_5$·nH$_2$O were attributed to V^{3+} (515.05 and 521.69 eV; 515.01 and 522.51 eV), V^{4+} (515.9 and 522.75 eV; 515.84 and 523.34 eV), and V^{5+} (517.2 and 524.33 eV; 517.11 and 524.61 eV) oxidation states.[60] It is evident that the major part of V 2p spectra consists of V^{5+}. The O 1s photoemission line was deconvoluted into three components. The two components of crystalline V$_2$O$_5$ located at 529.99 and 530.38 eV were attributed to the O^{2-} ions[61] and V−O linkage in the V$_2$O$_5$ while the component at 531.82 eV was assigned to the OH$^-$ groups.[62] These components of V$_2$O$_5$·nH$_2$O in XPS O 1s spectra were located at 529.92 eV, 530.94 eV, and 532.36 eV. The OH$^-$ group component is much more pronounced in the XPS O 1s spectra of V$_2$O$_5$·nH$_2$O due to its hydrated state.

Further, the TEM analysis of V$_2$O$_5$·nH$_2$O was performed for characterization of morphology. Figure S4 shows the TEM image of V$_2$O$_5$·nH$_2$O nanostructures formed via the melt-quenching process. The obtained nanostructures exhibited ribbonlike particle morphology,[46,63] which is in line with V. Petrikov et al.[27] The observed morphology of V$_2$O$_5$·nH$_2$O nanoribbons (Figure S4) is in good agreement with XRD results.

Characterization of GO. Figure S5 shows XRD diffraction pattern of GO. In the XRD diffraction pattern, the broad and distinct (0 0 1) reflex with a d-spacing of 7.9 Å was observable, indicating the presence of GO, consistent with results reported elsewhere.[64,65]

The Raman spectrum of GO is depicted in Figure S6. The deconvoluted G_1 and G_2 bands are located at 1596 cm^{-1} and 1545 cm^{-1}, while the D band is at 1350 cm^{-1}. The 2D and D+G bands are observed at 2697 and 2925 cm^{-1}, respectively. The statistical reliability factor (R^2) for fitting Gaussian components was found to be $R^2 \geq 0.97$. The D band arises from the defect-induced breathing modes of sp^2 rings.[66] The G_1 component is associated with the in-plane stretching vibration.[67] The G_2 component can be attributed to the bond angle disorder and surface functional groups (O−H).[66,68] The I_D/I_{G1}[69] and I_{G2}/I_{G1}[66] intensity ratios were found to be 0.98 and 0.52 for GO. The second order overtone, 2D, is due to the two-phonon double resonance, while the D+G band is attributed to higher structure disorder of GO.[70]

Chemical properties of GO were investigated using XPS. The XPS O 1s and C 1s high-resolution spectra are depicted in Figure S7. The first deconvoluted component at 531.2 eV in the O 1s spectrum (Figure S7a) is attributed to O−C=O, while the second and the third component at 532.4 and 533.6 eV to C−O and O−H chemical bonds.[71,72] Five deconvoluted components in the C 1s photoemission line (Figure S7b) located at 283.6 eV, 284.8 eV, 285.6 eV, 286.7 eV, and 288.3 eV were assigned to the C=C/C−C, C−C, C−O/C−O−C, C−O, and C=O chemical bonds, respectively.[64,72,73]

TEM image of GO is depicted in Figure S8. The GO flakes have a folded and corrugated sheet structure with numerous wrinkles. It can be observed, that the GO sheets are relatively large, indicating relatively low damage of the sheet structure produced by the mechanical stirring method.

Characterization of GO/V$_2$O$_5$·nH$_2$O and rGO/V$_2$O$_5$·nH$_2$O Nanocomposite Films. TEM inspection was performed for as prepared GO/V$_2$O$_5$·nH$_2$O nanocomposite and is depicted in Figure 1. It can be seen that V$_2$O$_5$·nH$_2$O nanoribbons are wrapped with GO sheets and are no longer easily distinguishable.
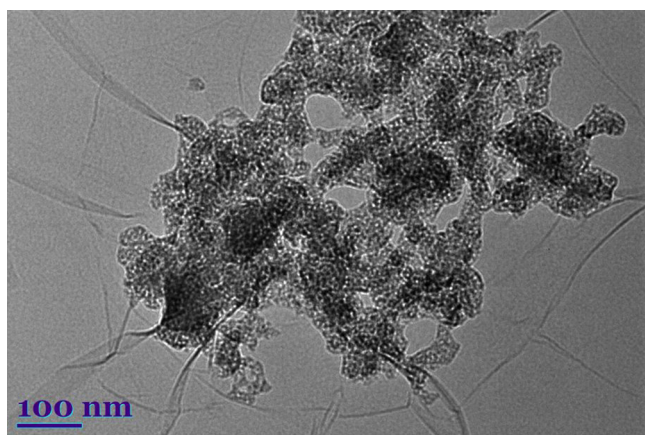

Figure 1. TEM micrograph of GO/V$_2$O$_5$·nH$_2$O nanocomposite.

SEM analysis was performed to inspect the surface features of GO/V$_2$O$_5$·nH$_2$O nanocomposite films. The SEM micrographs of GO/V$_2$O$_5$·nH$_2$O nanocomposite surface are shown in Figure 2, indicating a uniform and wrinkled surface of the film. It is known that GO can have different surface morphologies, which can be highly influenced by the pH of the system[74] and the deposition method.[75] It can be observed from the SEM images that the intersection of wrinkles assembled into starlike microstructures. Similar microstruc-
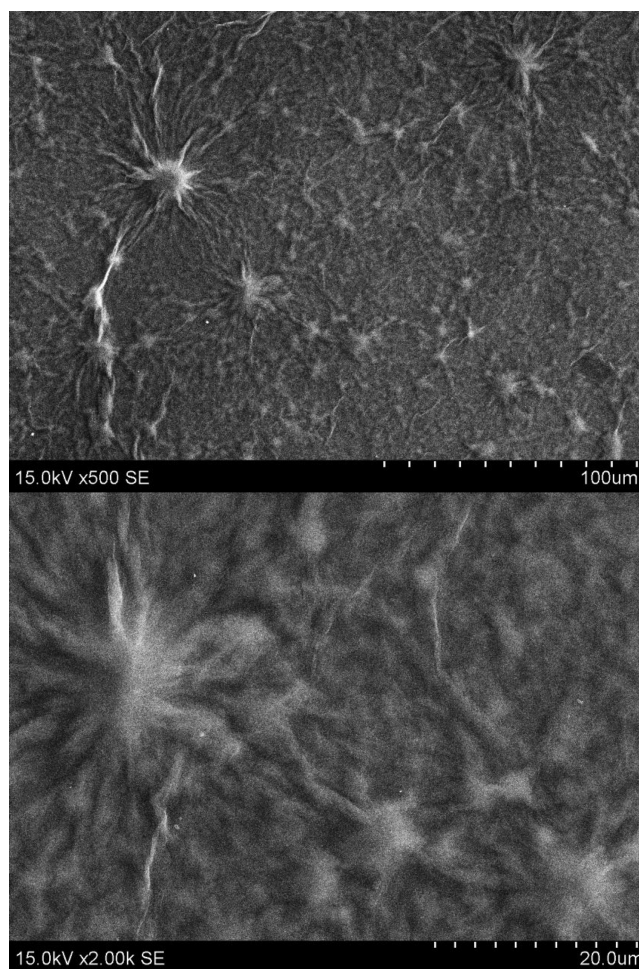

Figure 2. SEM micrographs at different magnification scale of GO/V$_2$O$_5$·nH$_2$O nanocomposite films.

tures were observed in our previous work,[42] where only GO films were studied. This is an indication that the resultant nanocomposite film morphology is mainly governed by GO sheets and V$_2$O$_5$·nH$_2$O nanoribbons in the system have no observable influence at this point. Additionally, SEM observations also imply that V$_2$O$_5$·nH$_2$O nanoribbons are not distinguishable from GO sheets on the surface of nanocomposite film, which is consistent with TEM results, that V$_2$O$_5$·nH$_2$O nanoribbons are wrapped with GO sheets.

Figure 3 shows SEM micrographs of rGO/V$_2$O$_5$·nH$_2$O nanocomposite films where direct laser irradiation took place in the grayish rectangle areas with LPD varied. In Figure 3a−d, LPD was varied in the range of 1.69−2.71 × 10^{5}W/cm^2. The rGO/V$_2$O$_5$·nH$_2$O areas in the SEM micrographs are easily distinguishable indicating that the photothermal modification process took place.

In contrast to GO/V$_2$O$_5$·nH$_2$O, the observed surface morphology of rGO/V$_2$O$_5$·nH$_2$O is significantly different. In all cases, the surface of rGO/V$_2$O$_5$·nH$_2$O is covered with randomly distributed pillarlike protrusions with the size in the range from several nanometers to tens of micrometers, exhibiting porous surface morphology. The specific surface area of rGO/V$_2$O$_5$·nH$_2$O was determined to be 17.27 m^2 g^{-1}, more than 4 times higher than that of GO/V$_2$O$_5$·nH$_2$O (3.84 m^2 g^{-1}). This is a very promising result considering LIB, supercapacitor, and sensor applications as it can improve the
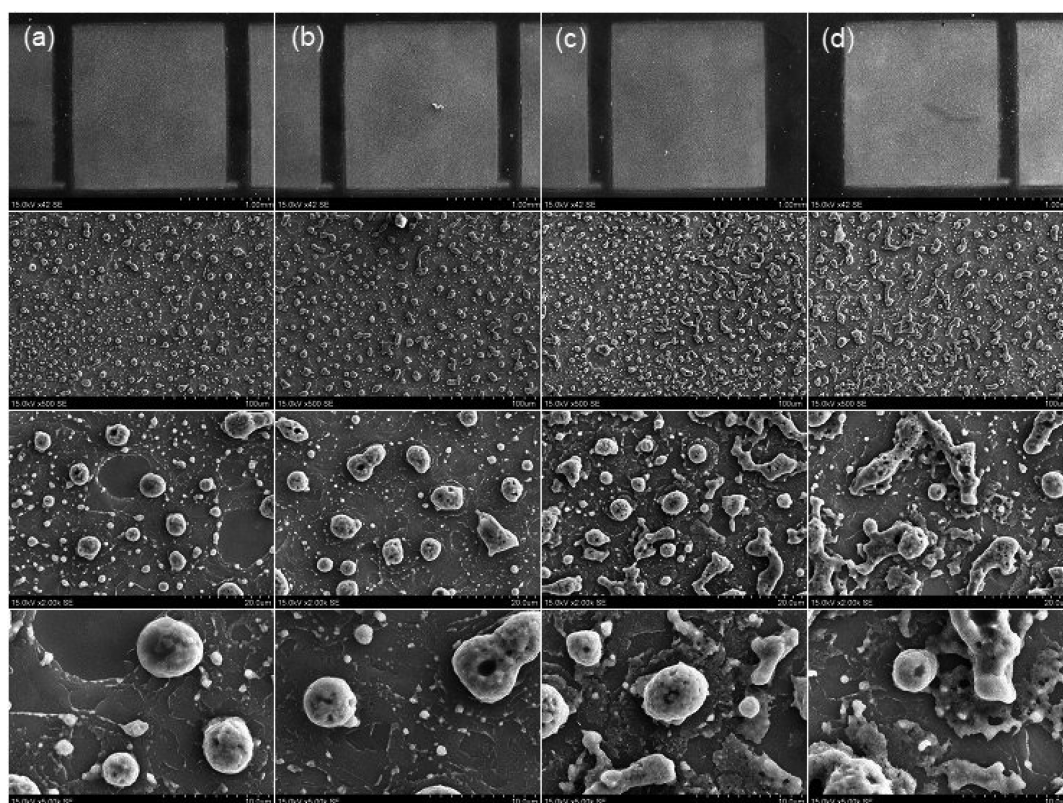
Figure 3. SEM micrographs at different magnification scales of rGO/V_2O_5·$n$$H_2O$ nanocomposite films. The direct laser irradiation took place in the grayish rectangle areas. LPD (a) 1.69, (b) 2.03, (c) 2.37, and (d) 2.71 × 10^5 W/cm^2 varied, respectively.
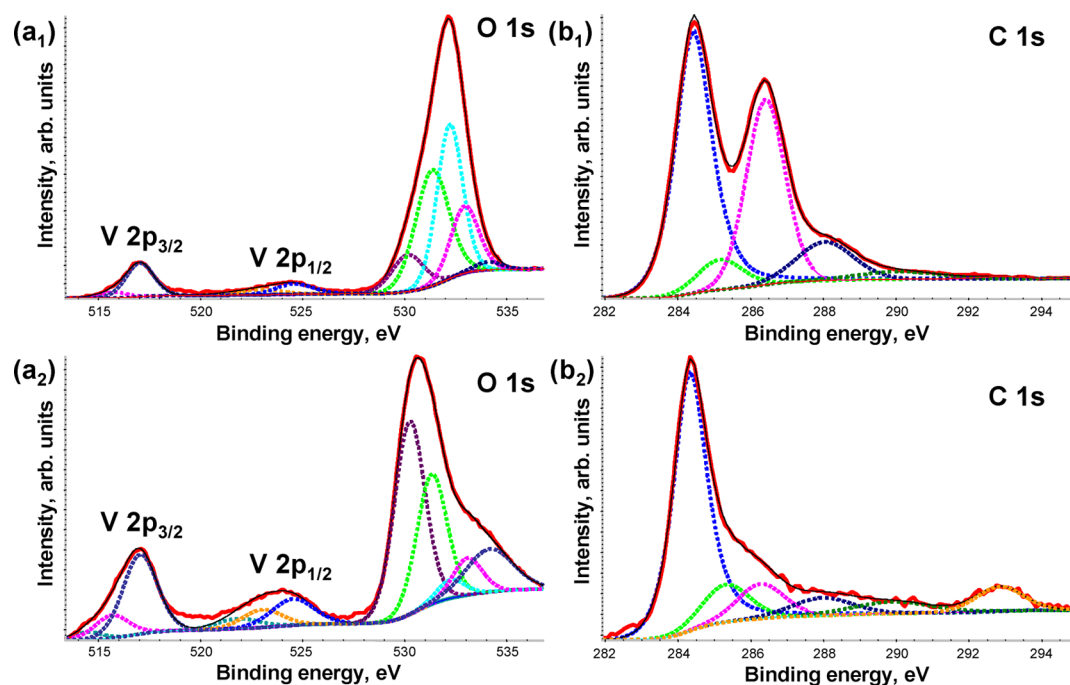

Figure 4. Deconvoluted high-resolution XPS: V 2p, O 1s, and C 1s spectra of (a_1 and b_1) GO/V_2O_5·$n$$H_2O$ and (a_2 and b_2) rGO/V_2O_5·$n$$H_2O$ nanocomposite films. Thick red lines show experimental data, thin black lines show the envelope, and thick dashed lines show the fitted components.

resultant energy storing capacity as well as sensor response with lower operating temperature and efficient detection characteristics. Importantly, SEM micrographs at 500× magnification (Figure 3) revealed morphological tendency,

which is dependent on the LPD: with the increase of LPD the pillarlike protrusions are prone to form clusters with increasing size. Quantitative data for morphological changes of cluster formation with LPD is depicted in Figure S9. Additionally, the

increase of LPD produced more nanometer-scale protrusions across the surface, e.g., from 2.37 to 2.71×10^5 W/cm^2 produced 12% more nanometer-scale protrusions. Fractional areas of all surface features constituted of 18.5 (1.69×10^5 W/cm^2), 18.6 (2.03×10^5 W/cm^2), 27.8 (2.37×10^5 W/cm^2), and 26.5% (2.71×10^5 W/cm^2). SEM observations suggest that photothermal modification of GO/V$_2$O$_5$·nH$_2$O results in formation of rGO/V$_2$O$_5$·nH$_2$O with heterogeneous surface morphology having a combination of micro- and nanoscale structural features.

The characteristic XRDGI pattern of rGO/V$_2$O$_5$·nH$_2$O nanocomposite film (LPD of 2.71×10^5 W/cm^2) is shown at Figure S10. After direct laser irradiation of GO/V$_2$O$_5$·nH$_2$O, the d-spacing for the (0 0 1) reflex of V$_2$O$_5$·nH$_2$O was found to be 10.3 Å, indicating removal of water molecules from the lattice with $n = 1.5$ (before modification $n = 1.7$). The crystallite size for the (0 0 1) reflection was found to be 54.4 Å, consistent with TEM. Another peak in the XRDGI pattern corresponds to rGO (0 0 2) reflex with d-spacing of 3.5 Å. The broadening in the rGO (0 0 2) indicates poor ordering of the stacked layers.

Figure S11 shows baseline-corrected Raman spectrum of rGO/V$_2$O$_5$·nH$_2$O nanocomposite film (LPD of 2.71×10^5 W/cm^2). It can be seen that Raman spectrum exhibits characteristic bands attributed to V$_2$O$_5$·nH$_2$O (104–1170 cm^{-1}) and rGO-deconvoluted bands by Gaussian components: G$_1$(1600 cm^{-1}), G$_2$(1535 cm^{-1}), D (1353 cm^{-1}), 2D (2714 cm^{-1}) and D+G (2936 cm^{-1}); $R^2 \geq 0.97$. The highest laser power density produced rGO in the nanocomposite system with I_D/I_{G1} and I_{G2}/I_{G1} ratios of 0.98 and 0.36. In contrast to GO, the considerable decrease in I_{G2}/I_{G1} ratio was observed for rGO, which indicates more ordered structure[67] and removal of functional groups.[68]

The I–V curves of GO/V$_2$O$_5$·nH$_2$O and rGO/V$_2$O$_5$·nH$_2$O (LPD of 2.71×10^5 W/cm^2) nanocomposite films are depicted in Figure S12. The I–V curve of rGO/V$_2$O$_5$·nH$_2$O nanocomposite shows ohmic characteristics which demonstrates that the photothermal modification process of GO/V$_2$O$_5$·nH$_2$O enhanced the conductivity of nanocomposite film. The electrical conductivity values for GO/V$_2$O$_5$·nH$_2$O and rGO/V$_2$O$_5$·nH$_2$O were determined to be 1.6 and 6.8 S/m. In contrast, V$_2$O$_5$ was reported to suffer from low electrical conductivity, which is in the range of 10^{-2}–10^{-3} S/cm.[28]

The effect of photothermal modification on the chemical states of GO/V$_2$O$_5$·nH$_2$O was investigated via XPS. The deconvoluted XPS V 2p, O 1s, and C 1s high-resolution spectra of GO/V$_2$O$_5$·nH$_2$O and rGO/V$_2$O$_5$·nH$_2$O (LPD of 2.71×10^5 W/cm^2) are shown in Figure 4. Similarly as in crystalline V$_2$O$_5$ and V$_2$O$_5$·nH$_2$O (Figure S3), the deconvoluted components of GO/V$_2$O$_5$·nH$_2$O and rGO/V$_2$O$_5$·nH$_2$O in the XPS V 2p$_{3/2}$ and V 2p$_{1/2}$ photoemission lines where assigned to V^{3+} (514.7 and 521.28 eV; 514.5 and 521.83 eV), V^{4+} (515.77 and 522.97 eV; 515.66 and 523.03 eV), and V^{5+} (517.02 and 524.58 eV; 517.03 and 523.03 eV) oxidation states.

The deconvoluted components of GO/V$_2$O$_5$·nH$_2$O and rGO/V$_2$O$_5$·nH$_2$O (LPD of 2.71×10^5 W/cm^2) in XPS O 1s spectra were assigned to V–O linkage in the V$_2$O$_5$(530.15 and 530.24 eV), O–C=O (531.35 and 531.33 eV), C–O (532.21 and 532.25 eV), and O–H (532.94 and 533.08 eV) chemical bonds.[62,70,72] The intensity decrease of C–O component at 532.25 eV for rGO/V$_2$O$_5$·nH$_2$O (Figure 4a$_2$) indicates the removal of carbon–oxygen bounds. The additional component of GO/V$_2$O$_5$·nH$_2$O and rGO/V$_2$O$_5$·nH$_2$O observed in XPS O 1s spectra at 534.09 and 534.18 eV is related to water molecules.[76–78] In the case of GO/V$_2$O$_5$·nH$_2$O, the latter component is significantly weaker as compared to rGO/V$_2$O$_5$·nH$_2$O, because H$_2$O molecules are tightly bound to their position in between GO and V$_2$O$_5$ layers. These XPS results are in line with the results reported in ref 79. Evolution of water molecules and changes in the O–H groups with LPD are summarized in Figure S13. The relative fraction of each component was calculated by dividing its area (A_x) by the total area (A_{Tot}) of all O 1s components. The deconvoluted components of GO/V$_2$O$_5$·nH$_2$O and rGO/V$_2$O$_5$·nH$_2$O in XPS C 1s spectra were assigned to C–C (284.41 and 284.31 eV), C–O/C–O–C (285.15 and 285.3 eV), C–O (286.41 and 286.26), C=O (288.03 and 287.95 eV), and O=C–OH (290.05 and 289.88 eV) bounds, and π–π* shakeup transition (292.9 and 292.85 eV), respectively.[80,81] Again, decreased intensity of the C–O component at 286.26 eV for rGO/V$_2$O$_5$·nH$_2$O (Figure 4b$_2$) indicates the removal of carbon–oxygen bounds. The summary of C–O chemical bond changes depending on the LPD for rGO/V$_2$O$_5$·nH$_2$O nanocomposite films is shown in Figure S14. Relative fraction of the C–O component was calculated by dividing the A_x by the A_{Tot} of all C 1s components. It is evident, that the removal of carbon–oxygen bounds took place up to the LPD of 2.03×10^5 W/cm^2. Afterward, the relative fraction of C–O chemical bonds remained steady at ∼0.1, indicating that no more breakup of carbon–oxygen bonds with increasing LPD. For GO/V$_2$O$_5$·nH$_2$O, the C–C/C–O ratio was determined to be 1.3, while after photothermal modification to rGO/V$_2$O$_5$·nH$_2$O with the LPD of 1.69×10^5 W/cm^2 it increased up to 5.0, indicating ∼83% conversion of GO to rGO. The GO reduction with the LPD of 2.03×10^5 W/cm^2 resulted in nearly complete restoration of aromatic π → π system with the C–C/C–O ratio of 5.98 (∼99% conversion of GO to rGO) remained steady in the range of 5.98–6.0 for higher laser power densities.

■ CONCLUSIONS

The photothermal modification of GO/V$_2$O$_5$·nH$_2$O via 405 nm direct laser irradiation has been studied. The nanocomposite system consisted of nanoribbons wrapped with graphene oxide (GO) flakes. The melt-quenching process produced V$_2$O$_5$·nH$_2$O nanoribbons having a monoclinic lattice, space group C 1 2/m1 (group number = 12) with a cell parameters $a = 11.700$ Å, $b = 3.617$ Å, $c = 11.447$ Å, $\alpha = \gamma = 90°$, $\beta = 88.07°$ and the (0 0 1), (1 1 0) reflexes observable. After direct laser irradiation of GO/V$_2$O$_5$·nH$_2$O via the d-spacing for the (0 0 1) reflex of V$_2$O$_5$·nH$_2$O was found to be 10.3 Å (before modification, 11.7 Å), indicating removal of water molecules from the lattice with $n = 1.5$ (before modification, $n = 1.7$). The XRD and Raman analyses confirmed that photothermal modification reduced GO to rGO as evident from broad (0 0 2) reflex in XRDGI pattern and decrease of I_{G2}/I_{G1} intensity ratio from 0.52 to 0.36 in Raman spectra. The rGO/V$_2$O$_5$·nH$_2$O nanocomposite films exhibited porous surface morphology (17.27 m^2 g^{-1}) consisting of randomly distributed pillarlike protrusions with the size in the range from several nanometers to tens of micrometers. It was determined that with the increase of LPD, the pillar-like protrusions are prone to form clusters with increasing size. The direct laser irradiation of GO/V$_2$O$_5$·nH$_2$O enhanced the electrical conductivity of nanocomposite from

1.6 to 6.8 S/m. It was determined that the photothermal modification process results in considerable decrease of C−O bounds as well as O−H functional groups with increase of LPD. The GO/V$_2$O$_5$·nH$_2$O nanocomposite can be further used in lithium−ion batteries, supercapacitors, and sensor applications.

■ ASSOCIATED CONTENT

Ⓢ Supporting Information

The Supporting Information is available free of charge at https://pubs.acs.org/doi/10.1021/acsami.0c02066.

> Materials and methods: formation of GO/V$_2$O$_5$·nH$_2$O nanocomposite films; photothermal modification of GO/V$_2$O$_5$·nH$_2$O nanocomposite films; characterization: XRD, Raman, XPS spectra as well as TEM images, and I−V curves; cluster formation dependence on LPD; evolution of water molecules and changes in O−H groups depending on LPD; and C−O chemical bond changes depending on the LPD (PDF)

■ AUTHOR INFORMATION

Corresponding Author

Algirdas Lazauskas − *Plasma Processing Laboratory, Lithuanian Energy Institute, LT44403 Kaunas, Lithuania; Institute of Materials Science, Kaunas University of Technology, LT51423 Kaunas, Lithuania;* ⓞ orcid.org/0000-0002-6633-2214; Phone: + 370-671-73375; Email: algirdas.lazauskas@ktu.lt

Authors

Liutauras Marcinauskas − *Plasma Processing Laboratory, Lithuanian Energy Institute, LT44403 Kaunas, Lithuania; Department of Physics, Kaunas University of Technology, LT-51368 Kaunas, Lithuania*

Mindaugas Andrulevicius − *Institute of Materials Science, Kaunas University of Technology, LT51423 Kaunas, Lithuania*

Complete contact information is available at:
https://pubs.acs.org/10.1021/acsami.0c02066

Notes

The authors declare no competing financial interest.

■ ACKNOWLEDGMENTS

■ REFERENCES

(1) Niu, C.; Li, J.; Jin, H.; Shi, H.; Zhu, Y.; Wang, W.; Cao, M. Self-template processed hierarchical V2O5 nanobelts as cathode for high performance lithium ion battery. *Electrochim. Acta* **2015**, *182*, 621−628.

(2) Liu, J.; Xia, H.; Xue, D.; Lu, L. Double-shelled nanocapsules of V2O5-based composites as high-performance anode and cathode materials for Li ion batteries. *J. Am. Chem. Soc.* **2009**, *131* (34), 12086−12087.

(3) Zhao, H.; Pan, L.; Xing, S.; Luo, J.; Xu, J. Vanadium oxides-reduced graphene oxide composite for lithium-ion batteries and supercapacitors with improved electrochemical performance. *J. Power Sources* **2013**, *222*, 21−31.

(4) Zhu, J.; Cao, L.; Wu, Y.; Gong, Y.; Liu, Z.; Hoster, H. E.; Zhang, Y.; Zhang, S.; Yang, S.; Yan, Q. Building 3D structures of vanadium pentoxide nanosheets and application as electrodes in supercapacitors. *Nano Lett.* **2013**, *13* (11), 5408−5413.

(5) Muster, J.; Kim, G. T.; Krstić, V.; Park, J. G.; Park, Y. W.; Roth, S.; Burghard, M. Electrical transport through individual vanadium pentoxide nanowires. *Adv. Mater. (Weinheim, Ger.)* **2000**, *12* (6), 420−424.

(6) Liu, J.; Wang, X.; Peng, Q.; Li, Y. Preparation and gas sensing properties of vanadium oxide nanobelts coated with semiconductor oxides. *Sens. Actuators, B* **2006**, *115* (1), 481−487.

(7) Qin, Y.; Fan, G.; Liu, K.; Hu, M. Vanadium pentoxide hierarchical structure networks for high performance ethanol gas sensor with dual working temperature characteristic. *Sens. Actuators, B* **2014**, *190*, 141−148.

(8) Liu, J.-f.; Wang, X.; Peng, Q.; Li, Y. Vanadium pentoxide nanobelts: highly selective and stable ethanol sensor materials. *Adv. Mater. (Weinheim, Ger.)* **2005**, *17* (6), 764−767.

(9) Yakovleva, D.; Malinenko, V.; Pergament, A.; Stefanovich, G. Electrical and optical properties of thin films of hydrated vanadium pentoxide featuring electrochromic effect. *Tech. Phys. Lett.* **2007**, *33* (12), 1022−1024.

(10) Oliveira, H. P.; Graeff, C. F.; Brunello, C. A.; Guerra, E. d. M. Electrochromic and conductivity properties: a comparative study between melanin-like/V2O5· nH2O and polyaniline/V2O5· nH2O hybrid materials. *J. Non-Cryst. Solids* **2000**, *273* (1−3), 193−197.

(11) Cheng, K.-C.; Chen, F.-R.; Kai, J.-J. V2O5 nanowires as a functional material for electrochromic device. *Sol. Energy Mater. Sol. Cells* **2006**, *90* (7−8), 1156−1165.

(12) Gu, G.; Schmid, M.; Chiu, P.-W.; Minett, A.; Fraysse, J.; Kim, G.-T.; Roth, S.; Kozlov, M.; Muñoz, E.; Baughman, R. H. V 2 O 5 nanofibre sheet actuators. *Nat. Mater.* **2003**, *2* (5), 316−319.

(13) Wang, Y.; Cao, G. Developments in nanostructured cathode materials for high-performance lithium-ion batteries. *Adv. Mater. (Weinheim, Ger.)* **2008**, *20* (12), 2251−2269.

(14) Wang, Y.; Takahashi, K.; Lee, K. H.; Cao, G. Nanostructured Vanadium Oxide Electrodes for Enhanced Lithium-Ion Intercalation. *Adv. Funct. Mater.* **2006**, *16* (9), 1133−1144.

(15) Mai, L.; Xu, X.; Xu, L.; Han, C.; Luo, Y. Vanadium oxide nanowires for Li-ion batteries. *J. Mater. Res.* **2011**, *26* (17), 2175−2185.

(16) Muhr, H. J.; Krumeich, F.; Schönholzer, U. P.; Bieri, F.; Niederberger, M.; Gauckler, L. J.; Nesper, R. Vanadium oxide nanotubes—a new flexible vanadate nanophase. *Adv. Mater. (Weinheim, Ger.)* **2000**, *12* (3), 231−234.

(17) Li, B.; Xu, Y.; Rong, G.; Jing, M.; Xie, Y. Vanadium pentoxide nanobelts and nanorolls: from controllable synthesis to investigation of their electrochemical properties and photocatalytic activities. *Nanotechnology* **2006**, *17* (10), 2560−2566.

(18) Pinna, N.; Willinger, M.; Weiss, K.; Urban, J.; Schlögl, R. Local structure of nanoscopic materials: V2O5 nanorods and nanowires. *Nano Lett.* **2003**, *3* (8), 1131−1134.

(19) Moretti, A.; Passerini, S. Bilayered nanostructured V2O5· nH2O for metal batteries. *Adv. Energy Mater.* **2016**, *6* (23), 1600868.

(20) Uchaker, E.; Zheng, Y.; Li, S.; Candelaria, S.; Hu, S.; Cao, G. Better than crystalline: amorphous vanadium oxide for sodium-ion batteries. *J. Mater. Chem. A* **2014**, *2* (43), 18208−18214.

(21) Grigorieva, A. V.; Badalyan, S. M.; Goodilin, E. A.; Rumyantseva, M. N.; Gaskov, A. M.; Birkner, A.; Tretyakov, Y. D. Synthesis, structure, and sensor properties of vanadium pentoxide nanorods. *Eur. J. Inorg. Chem.* **2010**, *2010* (33), 5247−5253.

(22) Jin, A.; Chen, W.; Zhu, Q.; Yang, Y.; Volkov, V. L.; Zakharova, G. S. Electrical and electrochemical characterization of poly (ethylene oxide)/V2O5 xerogel electrochromic films. *Solid State Ionics* **2008**, *179* (21−26), 1256−1262.

(23) Haber, J. Fifty years of my romance with vanadium oxide catalysts. *Catal. Today* **2009**, *142* (3−4), 100−113.

(24) Guerra, E. M.; Silva, G. R.; Mulato, M. Extended gate field effect transistor using V2O5 xerogel sensing membrane by sol-gel method. *Solid State Sci.* **2009**, *11* (2), 456−460.

(25) Su, L.; Winnick, J.; Kohl, P. Sodium insertion into vanadium pentoxide in methanesulfonyl chloride-aluminum chloride ionic liquid. *J. Power Sources* **2001**, *101* (2), 226−230.

(26) Fontenot, C.; Wiench, J.; Pruski, M.; Schrader, G. L. Vanadia gel synthesis via peroxovanadate precursors. 2. Characterization of the gels. *J. Phys. Chem. B* **2001**, *105* (43), 10496−10504.

(27) Petkov, V.; Trikalitis, P. N.; Bozin, E. S.; Billinge, S. J.; Vogt, T.; Kanatzidis, M. G. Structure of V2O5⊙ n H2O Xerogel Solved by the Atomic Pair Distribution Function Technique. *J. Am. Chem. Soc.* **2002**, *124* (34), 10157−10162.

(28) Pan, A.; Zhang, J.-G.; Nie, Z.; Cao, G.; Arey, B. W.; Li, G.; Liang, S.-q.; Liu, J. Facile synthesized nanorod structured vanadium pentoxide for high-rate lithium batteries. *J. Mater. Chem.* **2010**, *20* (41), 9193−9199.

(29) Mai, L.; Xu, L.; Han, C.; Xu, X.; Luo, Y.; Zhao, S.; Zhao, Y. Electrospun ultralong hierarchical vanadium oxide nanowires with high performance for lithium ion batteries. *Nano Lett.* **2010**, *10* (11), 4750−4755.

(30) Cao, A. M.; Hu, J. S.; Liang, H. P.; Wan, L. J. Self-assembled vanadium pentoxide (V2O5) hollow microspheres from nanorods and their application in lithium-Ion batteries. *Angew. Chem., Int. Ed.* **2005**, *44* (28), 4391−4395.

(31) Wu, J.; Gao, X.; Yu, H.; Ding, T.; Yan, Y.; Yao, B.; Yao, X.; Chen, D.; Liu, M.; Huang, L. A Scalable Free-Standing V2O5/CNT Film Electrode for Supercapacitors with a Wide Operation Voltage (1.6 V) in an Aqueous Electrolyte. *Adv. Funct. Mater.* **2016**, *26* (33), 6114−6120.

(32) Li, L.; Peng, S.; Wu, H. B.; Yu, L.; Madhavi, S.; Lou, X. W. A flexible quasi-solid-state asymmetric electrochemical capacitor based on hierarchical porous V2O5 nanosheets on carbon nanofibers. *Adv. Energy Mater.* **2015**, *5* (17), 1500753.

(33) Yu, L.; Zhao, C.; Long, X.; Chen, W. Ultrasonic synthesis and electrochemical characterization of V2O5/mesoporous carbon composites. *Microporous Mesoporous Mater.* **2009**, *126* (1−2), 58−64.

(34) Chen, D.; Yi, R.; Chen, S.; Xu, T.; Gordin, M. L.; Lv, D.; Wang, D. Solvothermal synthesis of V2O5/graphene nanocomposites for high performance lithium ion batteries. *Mater. Sci. Eng., B* **2014**, *185*, 7−12.

(35) Yao, L.; Zhang, C.; Hu, N.; Zhang, L.; Zhou, Z.; Zhang, Y. Three-dimensional skeleton networks of reduced graphene oxide nanosheets/vanadium pentoxide nanobelts hybrid for high-performance supercapacitors. *Electrochim. Acta* **2019**, *295*, 14−21.

(36) Perera, S. D.; Patel, B.; Nijem, N.; Roodenko, K.; Seitz, O.; Ferraris, J. P.; Chabal, Y. J.; Balkus, K. J., Jr. Vanadium Oxide Nanowire-Carbon Nanotube Binder-Free Flexible Electrodes for Supercapacitors. *Adv. Energy Mater.* **2011**, *1* (5), 936−945.

(37) Lee, J. W.; Lim, S. Y.; Jeong, H. M.; Hwang, T. H.; Kang, J. K.; Choi, J. W. Extremely stable cycling of ultra-thin V 2 O 5 nanowire-graphene electrodes for lithium rechargeable battery cathodes. *Energy Environ. Sci.* **2012**, *5* (12), 9889−9894.

(38) Ye, G.; Gong, Y.; Keyshar, K.; Husain, E. A.; Brunetto, G.; Yang, S.; Vajtai, R.; Ajayan, P. M. 3D Reduced Graphene Oxide Coated V2O5 Nanoribbon Scaffolds for High-Capacity Supercapacitor Electrodes. *Particle & Particle Systems Characterization* **2015**, *32* (8), 817−821.

(39) Wang, Y.; Shi, Z.; Huang, Y.; Ma, Y.; Wang, C.; Chen, M.; Chen, Y. Supercapacitor devices based on graphene materials. *J. Phys. Chem. C* **2009**, *113* (30), 13103−13107.

(40) Lee, M.; Balasingam, S. K.; Jeong, H. Y.; Hong, W. G.; Lee, H.-B.-R.; Kim, B. H.; Jun, Y. One-step hydrothermal synthesis of graphene decorated V 2 O 5 nanobelts for enhanced electrochemical energy storage. *Sci. Rep.* **2015**, *5*, 8151.

(41) Kumar, R.; Singh, R. K.; Singh, D. P.; Joanni, E.; Yadav, R. M.; Moshkalev, S. A. Laser-assisted synthesis, reduction and micropatterning of graphene: Recent progress and applications. *Coord. Chem. Rev.* **2017**, *342*, 34−79.

(42) Lazauskas, A.; Baltrusaitis, J.; Grigaliūnas, V.; Guobienė, A.; Prosyčevas, I.; Narmontas, P.; Abakevičienė, B.; Tamulevičius, S. Thermally-driven structural changes of graphene oxide multilayer films deposited on glass substrate. *Superlattices Microstruct.* **2014**, *75*, 461−467.

(43) Lazauskas, A.; Marcinauskas, L.; Andrulevicius, M. Photo-thermal reduction of thick graphene oxide multilayer films via direct laser writing: Morphology, structural and chemical properties. *Superlattices Microstruct.* **2018**, *122*, 36−45.

(44) Fakharan, Z.; Naji, L.; Madanipour, K. Surface roughness regulation of reduced-graphene oxide/iodine-Based electrodes and their application in polymer solar cells. *J. Colloid Interface Sci.* **2019**, *540*, 272−284.

(45) Shklover, V.; Haibach, T.; Ried, F.; Nesper, R.; Novak, P. Crystal Structure of the Product of Mg2+ Insertion into V2O5Single Crystals. *J. Solid State Chem.* **1996**, *123* (2), 317−323.

(46) Avansi, W., Jr.; Ribeiro, C.; Leite, E. R.; Mastelaro, V. R. Vanadium pentoxide nanostructures: an effective control of morphology and crystal structure in hydrothermal conditions. *Cryst. Growth Des.* **2009**, *9* (8), 3626−3631.

(47) Yao, T.; Oka, Y.; Yamamoto, N. Layered structures of hydrated vanadium oxides. Part 2.—Vanadyl intercalates (VO) x V 2 O 5· n H 2 O. *J. Mater. Chem.* **1992**, *2* (3), 337−340.

(48) Barbosa, G. d. N.; Graeff, C. F. d. O.; Oliveira, H. P. Thermal annealing effects on vanadium pentoxide xerogel films. *Ecletica Quim.* **2005**, *30* (2), 7−15.

(49) Ceccato, R.; Dirè, S.; Barone, T.; De Santo, G.; Cazzanelli, E. Growth of nanotubes in sol-gel-derived V 2 O 5 powders and films prepared under acidic conditions. *J. Mater. Res.* **2009**, *24* (2), 475−481.

(50) Wang, Y.; Shang, H.; Chou, T.; Cao, G. Effects of Thermal Annealing on the Li+ Intercalation Properties of V2O5⊙ n H2O Xerogel Films. *J. Phys. Chem. B* **2005**, *109* (22), 11361−11366.

(51) Wang, Y.; Cao, G. Synthesis and enhanced intercalation properties of nanostructured vanadium oxides. *Chem. Mater.* **2006**, *18* (12), 2787−2804.

(52) West, K.; Zachau-Christiansen, B.; Jacobsen, T.; Skaarup, S. Vanadium oxide xerogels as electrodes for lithium batteries. *Electrochim. Acta* **1993**, *38* (9), 1215−1220.

(53) Augustyn, V.; Dunn, B. Vanadium oxide aerogels: nano-structured materials for enhanced energy storage. *C. R. Chim.* **2010**, *13* (1−2), 130−141.

(54) Huila, M. F.; Parussulo, A. L.; Armas, L. E.; Peres, H. E.; Seabra, A. C.; Ramirez-Fernandez, F. J.; Araki, K.; Toma, H. E. Laser Patterning a Chem-FET Like Device on a V 2 O 5 Xerogel Film. *IEEE Sens. J.* **2018**, *18* (4), 1358−1363.

(55) Chauhan, P. S.; Bhattacharya, S. Highly sensitive V2O5· 1.6 H2O nanostructures for sensing of helium gas at room temperature. *Mater. Lett.* **2018**, *217*, 83−87.

(56) Mjejri, I.; Etteyeb, N.; Sediri, F. Hydrothermal synthesis of mesoporous rod-like nanocrystalline vanadium oxide hydrate V3O7· H2O from hydroquinone and V2O5. *Mater. Res. Bull.* **2013**, *48* (9), 3335−3341.

(57) Sethi, D.; Jada, N.; Tiwari, A.; Ramasamy, S.; Dash, T.; Pandey, S. Photocatalytic destruction of Escherichia coli in water by V2O5/TiO2. *J. Photochem. Photobiol., B* **2015**, *144*, 68−74.

(58) Wu, X.; Tao, Y.; Dong, L.; Hong, J. Synthesis and characterization of self-assembling (NH 4) 0.5 V 2 O 5 nanowires. *J. Mater. Chem.* **2004**, *14* (5), 901−904.

(59) Sharma, R. K.; Kumar, P.; Reddy, G. Synthesis of vanadium pentoxide (V2O5) nanobelts with high coverage using plasma assisted PVD approach. *J. Alloys Compd.* **2015**, *638*, 289−297.

(60) Ureña-Begara, F.; Crunteanu, A.; Raskin, J.-P. Raman and XPS characterization of vanadium oxide thin films with temperature. *Appl. Surf. Sci.* **2017**, *403*, 717−727.

(61) Iida, Y.; Venkatachalam, S.; Kaneko, Y.; Kanno, Y. X-ray Photoelectron Spectroscopic Study of Pulsed Laser Deposited V-W-Nd Mixed Oxide Films. *Jpn. J. Appl. Phys.* **2007**, *46* (5R), 3032.

(62) Glushenkov, A. M.; Hulicova-Jurcakova, D.; Llewellyn, D.; Lu, G. Q.; Chen, Y. Structure and capacitive properties of porous nanocrystalline VN prepared by temperature-programmed ammonia reduction of V2O5. *Chem. Mater.* **2010**, 22 (3), 914−921.

(63) Avansi, W.; Oliveira, C.; Ribeiro, C.; Leite, E.; Mastelaro, V. Study of the morphological evolution of vanadium pentoxide nanostructures under hydrothermal conditions. *CrystEngComm* **2016**, 18 (39), 7636−7641.

(64) Marcano, D. C.; Kosynkin, D. V.; Berlin, J. M.; Sinitskii, A.; Sun, Z.; Slesarev, A.; Alemany, L. B.; Lu, W.; Tour, J. M. Improved synthesis of graphene oxide. *ACS Nano* **2010**, 4 (8), 4806−4814.

(65) Jabbar, A.; Yasin, G.; Khan, W. Q.; Anwar, M. Y.; Korai, R. M.; Nizam, M. N.; Muhyodin, G. Electrochemical deposition of nickel graphene composite coatings: effect of deposition temperature on its surface morphology and corrosion resistance. *RSC Adv.* **2017**, 7 (49), 31100−31109.

(66) Aslam, S.; Mustafa, F.; Ahmad, M. A. Facile Synthesis of Graphene Oxide with Significant Enhanced Properties for Optoelectronic and Energy Devices. *Ceram. Int.* **2018**, 44 (6), 6823−6828.

(67) Shimodaira, N.; Masui, A. Raman spectroscopic investigations of activated carbon materials. *J. Appl. Phys.* **2002**, 92 (2), 902−909.

(68) Mowry, M.; Palaniuk, D.; Luhrs, C. C.; Osswald, S. In situ Raman spectroscopy and thermal analysis of the formation of nitrogen-doped graphene from urea and graphite oxide. *RSC Adv.* **2013**, 3 (44), 21763−21775.

(69) Matsubayashi, A.; Zhang, Z.; Lee, J. U.; LaBella, V. P. Microstructure fabrication process induced modulations in CVD graphene. *AIP Adv.* **2014**, 4 (12), 127143.

(70) Bîru, E. I.; Iovu, H. Graphene Nanocomposites Studied by Raman Spectroscopy. In *Raman Spectroscopy*; InTech, 2018; p 186,

(71) Jia, Z.; Li, C.; Liu, D.; Jiang, L. Direct hydrothermal reduction of graphene oxide based papers obtained from tape casting for supercapacitor applications. *RSC Adv.* **2015**, 5 (99), 81030−81037.

(72) Chen, C.-M.; Huang, J.-Q.; Zhang, Q.; Gong, W.-Z.; Yang, Q.-H.; Wang, M.-Z.; Yang, Y.-G. Annealing a graphene oxide film to produce a free standing high conductive graphene film. *Carbon* **2012**, 50 (2), 659−667.

(73) Mudila, H.; Rana, S.; Zaidi, M. Electrochemical performance of zirconia/graphene oxide nanocomposites cathode designed for high power density supercapacitor. *J. Anal. Sci. Technol.* **2016**, 7 (1), 3.

(74) Whitby, R. L. D.; Korobeinyk, A.; Gun'ko, V. M.; Busquets, R.; Cundy, A. B.; Laszlo, K.; Skubiszewska-Zieba, J.; Leboda, R.; Tombacz, E.; Toth, I. Y.; Kovacs, K.; Mikhalovsky, S. V. pH-driven physicochemical conformational changes of single-layer graphene oxide. *Chem. Commun. (Cambridge, U. K.)* **2011**, 47 (34), 9645−9647.

(75) Pandey, D. K.; Chung, T. F.; Prakash, G.; Piner, R.; Chen, Y. P.; Reifenberger, R. Folding and cracking of graphene oxide sheets upon deposition. *Surf. Sci.* **2011**, 605 (17−18), 1669−1675.

(76) Buchsteiner, A.; Lerf, A.; Pieper, J. Water dynamics in graphite oxide investigated with neutron scattering. *J. Phys. Chem. B* **2006**, 110 (45), 22328−22338.

(77) Dreyer, D. R.; Park, S.; Bielawski, C. W.; Ruoff, R. S. The chemistry of graphene oxide. *Chem. Soc. Rev.* **2010**, 39 (1), 228−240.

(78) Ossonon, B. D.; Bélanger, D. Synthesis and characterization of sulfophenyl-functionalized reduced graphene oxide sheets. *RSC Adv.* **2017**, 7 (44), 27224−27234.

(79) Rabchinskii, M. K.; Shnitov, V. V.; Dideikin, A. T.; Aleksenskii, A. E.; Vul', S. P.; Baidakova, M. V.; Pronin, I. I.; Kirilenko, D. A.; Brunkov, P. N.; Weise, J.; Molodtsov, S. L. Nanoscale perforation of graphene oxide during photoreduction process in the argon atmosphere. *J. Phys. Chem. C* **2016**, 120 (49), 28261−28269.

(80) Bertóti, I.; Mohai, M.; László, K. Surface modification of graphene and graphite by nitrogen plasma: Determination of chemical state alterations and assignments by quantitative X-ray photoelectron spectroscopy. *Carbon* **2015**, 84, 185−196.

(81) Kwan, Y. C. G.; Ng, G. M.; Huan, C. H. A. Identification of functional groups and determination of carboxyl formation temperature in graphene oxide using the XPS O 1s spectrum. *Thin Solid Films* **2015**, 590, 40−48.